
Article:
Deng, F., Xie, F., Qin, N. orcid.org/0000-0002-6437-9027 et al. (3 more authors) (2018) Drag reduction investigation for hypersonic lifting-body vehicles with aerospike and long penetration mode counterflowing jet. Aerospace Science and Technology, 76. pp. 361-373. ISSN 1270-9638

https://doi.org/10.1016/j.ast.2018.01.039

Drag reduction investigation for hypersonic lifting-body vehicles with aerospike and long penetration mode counterflowing jet

Fan Deng[a,b], Feng Xie[b,d], Ning Qin[b], Wei Huang[c], Lansong Wang[a,e], Hongyu Chu[a]

[a] Science and Technology on Space Physics Laboratory, China Academy of Launch Vehicle Technology, Beijing 100076, China

[b] Department of Mechanical Engineering, University of Sheffield, Sheffield S1 3JD, UK

[c] Science and Technology on Scramjet Laboratory, National University of Defense Technology, Changsha, Hunan 410073, China

[d] Hypervelocity Aerodynamics Institute, China Aerodynamics Research and Development Center, Mianyang Sichuan 621000, China

[e]Department of Mechanical & Aerospace Engineering, University of Strathclyde, Glasgow G1 1XJ, UK

Abstract: This study describes numerical computations of aerospike and counterflowing jet as drag reduction methods for a hypersonic lifting-body model for Mach 8 flow at 40 km altitude. The three-dimensional Navier-Stokes equation and the laminar condition have been utilized to obtain the flow field properties. Both steady-state and time-accurate computations are performed for the models in order to investigate the drag reduction effect and the periodic oscillation characteristics of long penetration mode (LPM) jet. Results showed that both of them can significantly modify the external flowfields and strongly weaken or disperse the shock-waves of the vehicle, then achieve an obvious drag reduction effect in the range of small angles of attack. The value is 7.25% for model with aerospike and 8.80% for model with counterflowing jet at angle of attack of 6 degree. Compared with aerospike, counterflowing jet shows a better drag reduction effect in the gliding angle of attack, and this leads to a larger lift-to-drag ratio of 3.58. Meanwhile, the displacement of center of pressure of the whole vehicle is smaller in the flight phase. The oscillation frequency of the counterflowing jet at angle of attack of 6 degree is 444Hz, and the oscillation characteristics of drag is due to the change of the pressure distribution caused by the oscillation of the shock structure. The results may be of high practical significance and show the possibility of developing a feasible system using counterflowing jet as an active flow control of reducing drag during hypersonic vehicle gliding with maximum lift-to-drag ratio.

Keywords: hypersonic; lifting-body vehicle; drag reduction; aerospike; counterflowing jet

Nomenclature

D	= vehicle nose diameter, mm
L	= vehicle length, mm
L_1	= first cone length, mm
L_2	= second cone length, mm
Φ_1	= first cone base diameter, mm
Φ_2	= second cone base diameter, mm
S	= span of the triangular wings, mm
χ	= leading edge swept angle of the wing, °
P	= static pressure, Pa
P_0	= inflow total pressure, Pa
P_{0f}	= freestream total pressure behind shock wave, Pa
P_{oj}	= jet total pressure, Pa
P_j	= jet static pressure, Pa
P_∞	= inflow static pressure, Pa
Ma	= Mach number
Re_L	= unit Reynolds number
α	= angle of attack, °
C_D	= drag force coefficient
C_L	= lift force coefficient
k	= lift-to-drag ratio
X_{cp}	= pressure center coefficient

1. Introduction

In the design of hypersonic vehicles with long time flight in near space, the lifting-body is one of the main aerodynamic configurations due to its good lift-to-drag ratio and internal loading space. The vehicle nose is subjected to severe aerodynamic heating and strong shock wave drag during high speed flight, contributing disproportionately to the vehicle drag and aerothermal loads, which translate into poor aerodynamic performance and stringent thermal protection system requirements, and other performance penalties including vehicle range, weight and payload. Thus, a variety of techniques have been implemented, and these techniques include aerospike[1][2][3], counterflowing jet [4][5][6] and energy deposition [7]. But the power budget and the system complexity are highly prohibitive for using the energy deposition concept. In addition, the high temperature gas produced by local energy deposition probably imposes a heavier burden on the design of thermal protection systems for hypersonic vehicles. For this reason, at present, the main methods of drag reduction for hypersonic vehicle are aerospike and counterflowing jet [8][9], and Wang et al. [10] gave a detail review on the experimental investigation on drag and heat flux reduction in supersonic/hypersonic flows in 2016.

A hypersonic lifting-body vehicle yields a strong detached bow shock wave ahead of it [11]. This shock wave is responsible for the elevated pressure levels attained by the downstream flow. Thus, it was believed that the excessive drag can be reduced by altering the flow field pattern ahead of the vehicle nose so as to eliminate the strong shock wave or replace it with a weaker system of shock waves. Early research focused on flow mechanism around the spike, Mair [12] experimentally examined the supersonic flow around spiked flat cylindrical and hemisphere cylindrical models, recorded a sign of flow instability around spiked bodies, and proposed the first explanation of this form of ”flow oscillation” based on the pressure difference between the flow downstream of the reattachment shock and the flow inside the recirculation zone. Maull [13] refined the mechanism of boundary layer separation over the spike length based on the pressure equilibrium on both sides of the separation shock wave, and he also clarified the mechanism of flow stability based on the mass flow equilibrium between the flow scavenged by the shear layer and that reversed inside the dead air zone. The governing factor was argued to be the flow turning angle on the model’s face at reattachment point. Wood [14]used the term ”dividing streamline” to refer to the streamline that links the separation and reattachment points of the share layer at steady flow conditions. At the same time, Chapman et al. [15]

argued that if the total pressure of the dividing streamline equals the peak pressure downstream of reattachment shock, the dividing streamline stagnates on the forebody and a stable shear layer is attained. Ahmed and Qin [16][17][18] found both spike length and aerodisk diameter dictate the flow mode, and the flow around the spiked model can be stable if the main geometric parameters is reasonable designed. This gives the researchers motivation to optimize the spike in order to achieve the best drag reduction effect in a stable flow structure.

Spike geometric parameters such as spike length, aerodisk geometry, forward body geometry and relative spike diameter were studied for drag reduction effect [19][20][21]. Some researchers [22][23][24] investigated the aerodynamic characteristics of conical, hemispherical, flat-faced aerospike, and hemispherical and flat-faced disk attached to the aerospike, and they found that the aerodisk spike has a superior drag reduction capability as compared to the other aerospikes. The effects of the spike length, shape, spike nose configuration and angle of attack on the reduction of the drag were experimentally studied by Kalimuthu et al. [25], and they found that the aerodisk with L/D = 2.0 is most effective among the models tested. Yadav and Guven [26] proved numerically that double-disk aerospikes are superior to single disk aerospikes of same overall length and hemispherical cap size in reducing drag of the main body. To study the aerodynamic characteristic of spike at a certain angle of attack, Schülein [27] introduced the concept of ”pivoting spike” in which the spike is maintained aligned with the freestream direction while the whole body is at incidence. He experimentally examined the pivoting spike in Mach 2, 3 and 5 with up to 30° incidence angle, and the experimental results presented show clearly the advantages of the aligned spikes over the conventional fixed spikes.

Another drag reduction method is a counterflowing jet in the stagnation zone of the vehicle [28], and the large scale vortices develop gradually in a recirculation zone when the jet terminates through a Mach disk and reverses its orientation as a conical free shear layer. The recirculation zone ahead of the vehicle has a great impact on reduction of the drag force [29].

Finley [30] performed a series of experiments in which a jet issues from an orifice at the nose of a body in supersonic flow to oppose the mainstream and developed an analytical model of the flow which suggests that the aerodynamic features of a steady flow depend primarily on a jet flow-force coefficient, and the Mach number of the jet in its exit plane. The transition between LPM(Long Penetration Mode) and SPM(Short Penetration Mode) was abrupt and was shown to occur at various PR(jet total pressure ratio) depending on body size and the jet exit Mach number [31]. Josyula et al.

[32]investigated the potential applications of a counterflowing drag reduction technique to assess performance improvements on aerospace vehicles. It was demonstrated that 30-50% drag reduction can be achieved by counterflowing blowing against a supersonic stream of Mach 4 or higher. Liet al. [33] investigated the drag reduction mechanism in supersonic blunt body with different jet strategies, and they found that taking the drag reduction and heat protection into consideration together, the effect of square shape is the best in all considered strategies.

Bushnell and Huffman [34] studied long penetration jet interactions and observed that the transition from LPM to SPM occurred at fixed PR for all engine sizes tested. Shang et al. [35][36] focused on the pressure ratio, which is describing the counter flow jet phenomenon, and they discovered the shock bifurcation phenomenon and shock-wave interaction by experimental and computational studies. Fomichev et al. [37] experimental and numerical studied the impact of counterflowing plasma jets on integral and distributed aerodynamic characteristics of blunted bodies in hypersonic flows with a counterflowing plasma jet, and a decrease in the total-drag coefficient for a 60^{o}-cone up to 25% at the LPM regime was obtained.

Kulkarni et al. [38] demonstrated reduction in aerodynamic drag for blunt cone flying at hypersonic Mach number by heat addition into the shock layer in shock tunnel, and the experimental data shown about 47% reduction in aerodynamic drag for a chromium plated 60° apex angle blunt cone in Mach 8 hypersonic flow. Aruna and Anjalidevi [39] investigated the effect of counterflowing jet on reduction of drag around two blunt cone flare bodies in the hypersonic turbulent flow at Mach number of 6.5, and comparing the values pertained to the case in the absence of jet, substantial reductions in total drag around 37.54%.

Most of the above studies mainly focus on the influence of the drag reduction technologies on nose with different shapes, rarely involve the whole vehicle, especially the drag reduction effect of vehicle in flight angle of attack, which is the reason for writing this article.

The present effort consists of two parts, namely vehicle with aerospike and vehicle with counterflowing jet. The numerical simulations are generated by solving the three-dimensional, compressible Navier–Stokes equations based on structured and hybrid mesh approach. The calculations are concentrated in drag reduction effect and aerodynamic characteristics of the vehicle. In addition to comparison of drag reduction effect of the two methods, the other focus of the present study is to perform more detailed time-accurate computations for unsteady calculation in an attempt to

explore the periodic variation of LPM counterflowing jet, since flow instability plays a crucial role for its drag reduction. For the first time, we studied the periodic oscillation characteristics of counterflowing jet on the nose of hypersonic vehicle at the cruising angle. All the obtained results have more practical value for the engineering application of the two approaches.

2. Design scheme and numerical method

2.1 Geometry for models

In order to explore the influence of the presence of aerospike and counterflowing jet on the reduction of total drag of the lifting-body vehicle flying at hypersonic speeds at an altitude of 40 km and Mach 8, three calculation models are established, namely one is the baseline model, and the other two are models with aerospike and counterflowing jet.

The geometric shape of baseline model is a two cone body, see Fig. 1. The two cone body of the vehicle has a length of 3000mm. The first cone has a base diameter of 300mm and length of 700mm, the second cone has a base diameter of 450mm and length of 2300mm, and the span of the triangular wings is 1500mm with the same length as the second cone and the leading edge swept angle of the wing is 75.6°. The nose of the vehicle is a spherical cap with diameter of D=100mm.

Model with aerospike has a 2D length and 0.1D diameter sting, the diameter of the inverted triangle shape disk is 0.3D, while model with counterflowing jet has a circular-shaped jet with a diameter of 0.1D at the center of nose and the medium of flow is selected as air. The geometry of the vehicle with aerospike and counterflowing jet are shown in Fig. 2.

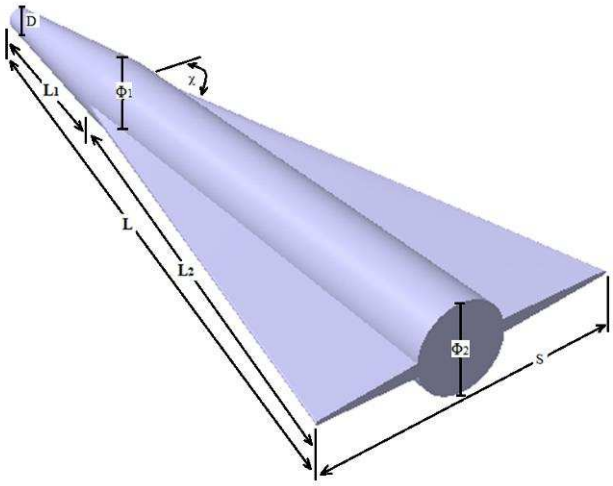

Fig. 1 Baseline model.

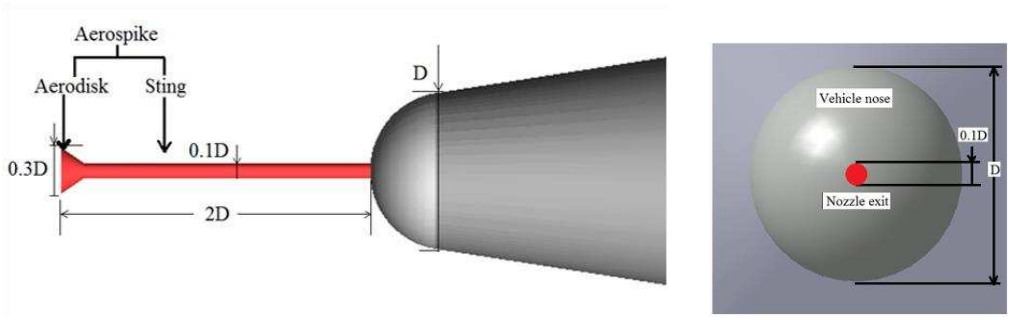

(a) With aerospike (b) With counterflowing jet

Fig. 2 Enlarged views of vehicle nose with different drag reduction technologies.

2.2 Computational meshes

Different mesh strategies are used for these models, which can be seen in Fig. 3 below. Structured mesh is applied for baseline model and model with aerospike. The meshes are multi-block-structured mesh, and the mesh sizes are 6.0 million and 8.0 million, respectively. Most of the nodes are clustering near the nose and the spike to capture the details of low pressure recirculation zone for model with aerospike.

For model with counterflowing jet, it should be noticed that capturing LPM jets requires an extremely fine mesh, hybrid mesh is generated because of the complex flow around the vehicle, mesh before the nose are equivalent geometric scaled unstructured mesh, the mesh remain almost uniform in size, which has been proved that the jet flow can be simulated well by this method. The density of the mesh is much higher than that of the body mesh, and this is crucial to maintaining the accuracy of the simulation since the flow structure of the nose has an important influence on the aerodynamic characteristics of the whole vehicle.

Multi-block-structured mesh is applied for the vehicle wings and body, and the mesh is highly concentrated close to the wall surfaces in order to ensure the accuracy of the numerical simulation. The height of first cell from the wall is 5×10^{-5} m to resolve the boundary layer shear near the wall. Y^+ over the wall surface of the nose was kept below 0.5 to a maximum of 4.0. The final mesh count was approximately 15.07 million cells.

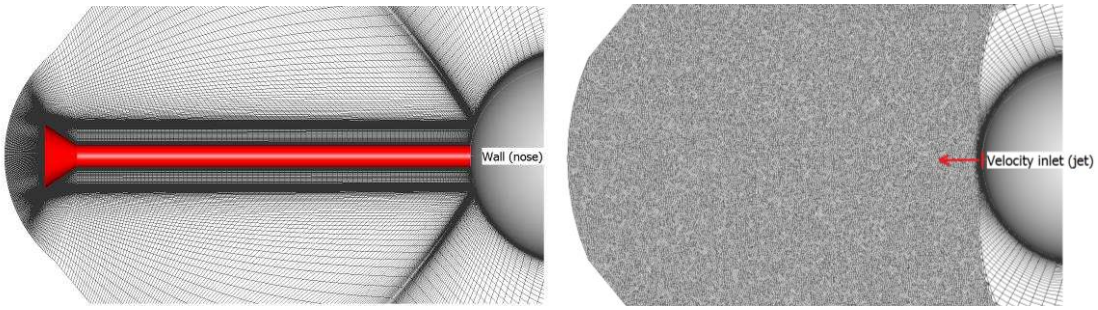

(a) Structured mesh near the nose with aerospike

(b) Hybrid mesh near the nose with counterflowing jet

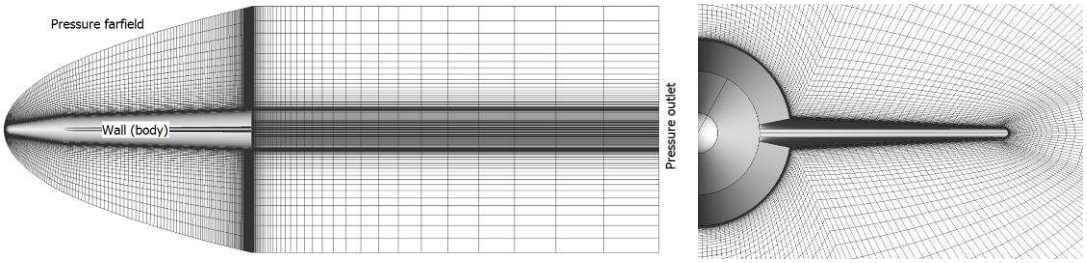

(c) Symmetry-boundary mesh

(d) Wing-body mesh

Fig. 3 Computation area and mesh distribution.

2.3 Numerical methods

At an altitude of 40 km, the static pressure and static temperature of the freestream are 287Pa and 250K, respectively. Accordingly, the Reynolds number is $Re_L=1.7\times10^6$ based on the base diameter of the second cone and the free stream velocity. At this Reynolds number, the flow can be assumed as laminar flow. Thus, the simulations are all in laminar. For baseline model and model with aerospike, the 3-D steady Navier-Stokes equations in the laminar condition are employed to simulate the flow field. For the counterflowing jet case, a 3-D unsteady Navier-Stokes equations in the laminar condition are employed, subsequent to the initial steady state solution, unsteady analyses were performed by introducing the counterflowing jet ejected from the central point of the nose into the upstream flow.Based on the convergent steady results, unsteady numerical computation has 20 pseudo time steps, and physical time step size is 1×10^{-5}s, the total physical steps is 3950.

With suitable under-relaxation factors, the Courant–Friedrichs–Levy (CFL) number is set as 0.01 at first and increases to 0.3 with the progress of convergence to ensure stability. The solutions can be considered as converged when all the residuals reach their minimum values after falling for more than five orders of magnitude [40][41].

For baseline model and model with aerospike, there are three kinds of boundary conditions in the simulations, including no-slip adiabatic wall, pressure farfield and pressure outlet. For model with counterflowing jet, in addition to these boundary conditions, the counterflowing jet is added and considered to be the velocity inlet. The jet air is assumed to be the perfect gas, and the jet pressure ratio(PR) is defined as follows:

$$PR = P_{0j} / P_{0f}$$

Herein, P_{0j} is the total pressure of the jet and P_{0f} is the freestream total pressure behind normal

shock wave. The flow conditions for the computations performed are summarized in Table 1.

Table 1 Flow condition of free stream and counterflowing jet.

Contents	Symbol	Unit	Value
Freestream Mach number	Ma	-	8
Freestream total pressure behind shock wave	P_{0f}	Pa	23794
Freestream static temperature	T_{∞}	K	250
Jet Mach number	Ma_j	-	2
Jet pressure ratio	PR	-	3.91
Jet total temperature	T_{0j}	K	300

The aerodynamic coefficients and the position of pressure center are obtained by the reference length of 3m and reference area of $0.2m^2$ which are based on the length of main body and the area of the second cone base, respectively. The origin of the coordinates system is set at the top central point of vehicle nose for all the models.

2.4 Validation of numerical methods

In order to validate the credibility of the numerical methods employed in this paper, the numerical methods and mesh generation strategy were adopted to verify different models from the published literature.

An experimental case by Kalimuthu et al. [42] is used for the verification of model with aerospike. The experimental model has a blunt body installed with a hemispherical aerospike at the nose. The diameter of the hemispheric disk was 0.1D, and the length of the spike was 2D. In this case, the incoming flow conditions were freestream Mach number of 6, stagnation pressure of 830,000Pa and stagnation temperature of 450K. Structured mesh is used in numerical calculation. A density gradient contour of the simulation is compared with the Schlieren photograph of the experiment in Fig. 4(a). The foreshock, recirculation region and shear layer are captured around the model. The drag coefficients were obtained at different angles of attack, from 0°~8°. Fig. 5(a) shows the comparison of drag coefficients at different angles of attack. Comparing the simulation outcomes with the experimental results, the error turns out to be less than 4.2%.

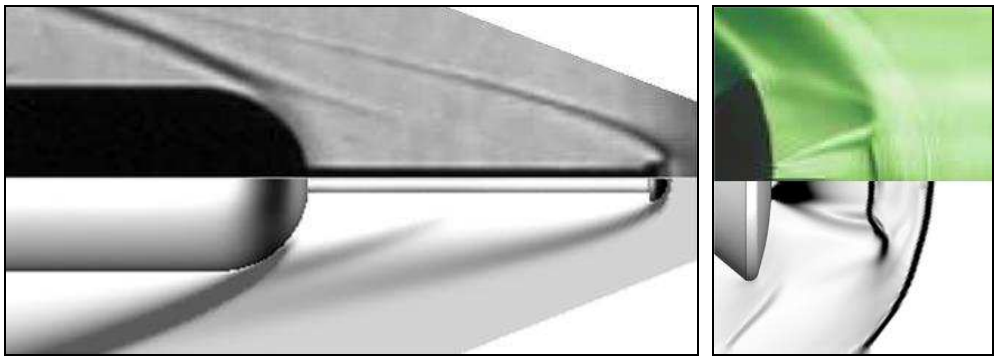

(a) Aerospike (b) Counterflowing jet

Fig. 4 Comparison of experimental Schlieren photograph (upper) and computed density gradient contour(lower).

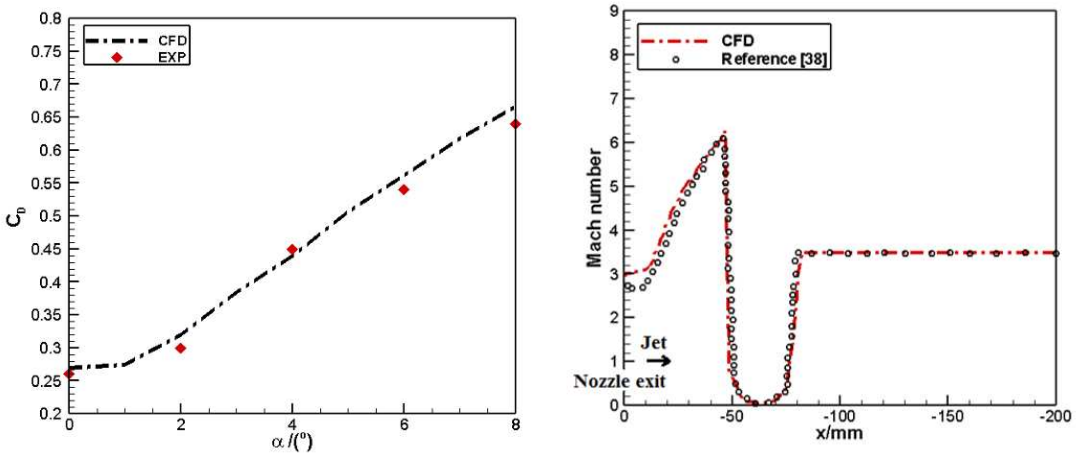

(a) Drag coefficients (b) Shock stand-off distance

Fig. 5 Comparison of the experimental and CFD data.

For the numerical calculation of counterflowing jet using hybrid mesh strategy, a three dimensional axisymmetric 2.6%-scale Apollo capsule model with zero angle of attack is used for verification. The same model was studied experimentally by Daso et al. [43]. For the far field, the undisturbed free-stream condition at the upstream is specified as: M_∞=3.48, P_∞=4201Pa, T_∞=94.2K. Viscous, non-slip and constant temperature condition are applied on the body surface. At the jet exit, the jet total temperature is 284.2 K, and Mach number is 2.94.

Fig. 4(b) shows a qualitative comparison of the CFD prediction and the Schlieren image of the interaction between the Mach 3.48 free-stream and Mach 2.94 jet at a flow rate of 0.215kg/s. This complex interacting flow field constitutes a new displacement shape with jet pushing the bow shock standing away from the body surface, there is Mach reflection at the jet exit and Mach disk is shown. The shock stand-off distance is consistent with the CFD results of Ref.[46] as Fig.5 (b) shown.

Based on the preceding expression, the results prove that numerical method is satisfactory to

investigate the performance of model with the two drag reduction strategies.

3. Results and Discussion

The results of this study are illustrated by the curves of pressure distributions on the noses of the models, drag coefficients and aerodynamic characteristics of the models. Firstly, pressure distributions on the noses of different models are compared. Then, drag coefficients of models with aerospike and counterflowing jet are shown to study the drag reduction effect, the lift-to-drag ratio and center of pressure of the models are analyzed as well. Finally in this section, periodic oscillation characteristics of LPM counterflowing jet at the cruising angle of attack are utilized to investigate the flow field structure variation in a cycle.

3.1 Pressure distribution

Initial computations were started without jet to set a base line or standard case against which the results with aerospike and jet could be analyzed. The results for the baseline model case, as expected, showed the formation of a strong detached bow shock wave ahead of the nose of the model, as shown in Fig. 6, The aerospike generates the recirculation regions and prevents constructing strong recompressed shocks in front of the nose, while the counterflowing jet interacts with the oncoming hypersonic flow, which causes the bow shock to move away from the nose and takes the form of a new body shape. In order to carry out comparative study, details of the flow structure at angle of attack of zero degree are illustrated with the close-up view in Fig. 7. As we can see, the flow field near the nose of model with the aerospike is similar to that with counterflowing jet. Enlarged image of nose with counterflowing jet shows that the streamlines below the dividing streamline pass downstream, whereas the streamlines above it are trapped inside the recirculation zone. As shown in Fig. 8, compared with the pressure of baseline model, the flow pressure is greatly reduced and maintains a near constant value in the entire recirculation zone for both cases. Then, as the shear layer approaches the nose shoulder, the flow decelerates through a compression wave, causing the pressure to increase in the vicinity of the reattachment point. The curved surface of the hemispherical body causes the flow to expand downstream of the reattachment point through an expansion wave, the surface pressure decreases toward the main body shoulder. The pressure increases rapidly with the increasing of angle of attack, when angle of attack is 8 degree, the maximum values of pressure of the two models' nose are close to the maximum value of the baseline model.

The static pressure distributions on the nose surface of model with aerospike and counterflowing jet vary with angle of attack, see Fig. 9. Excluding angle of attack of zero degree, the pressure on the surface with counterflowing jet is obviously less than that with aerospike taking the peak values of pressure and the area of high pressure as evaluation criteria.

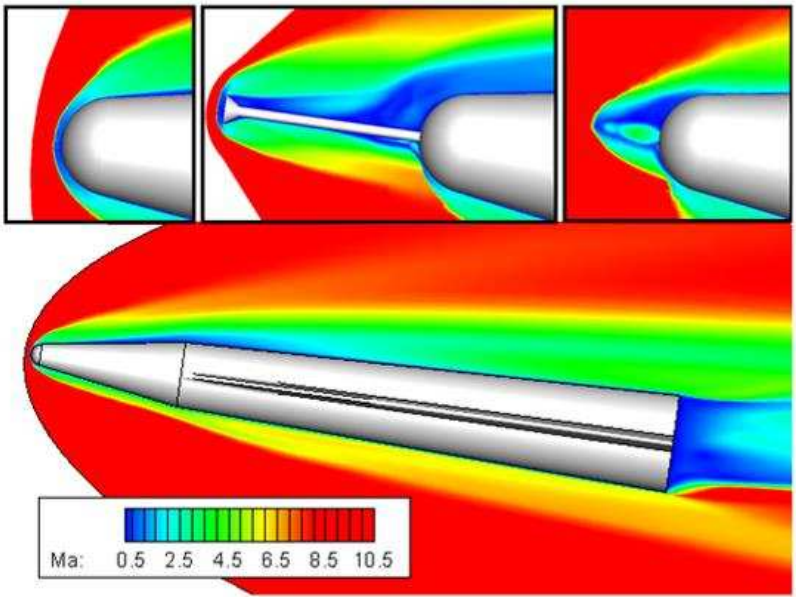

Fig.6 Comparison of Mach number distribution of vehicle with different drag reduction techniques (a=8°).

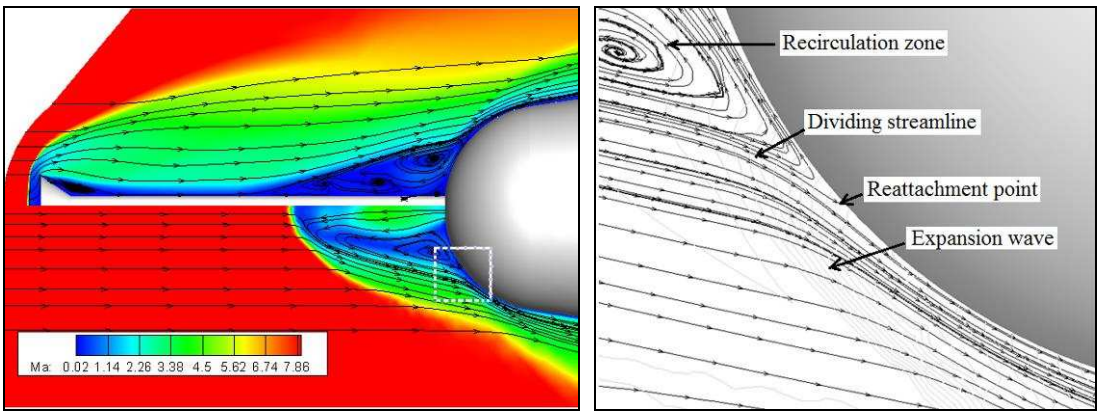

(a) Aerospike(upper) and counterflowing jet(lower) (b) Shoulder of vehicle nose

Fig.7 Flow structure around vehicle nose and its shoulder (a=0°).

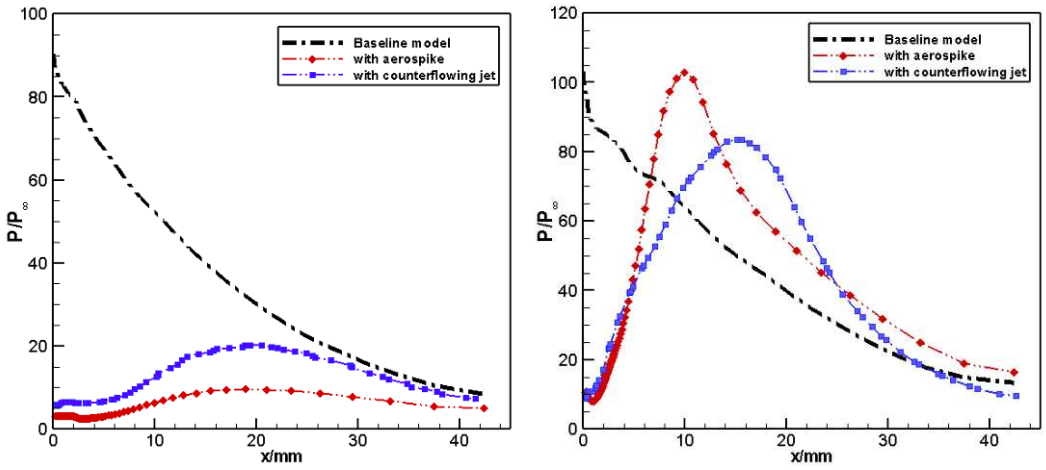

（a）α=0º　　（b）α=8º

Fig. 8 Non-dimensional pressure distribution on symmetrical plane of vehicle nose.

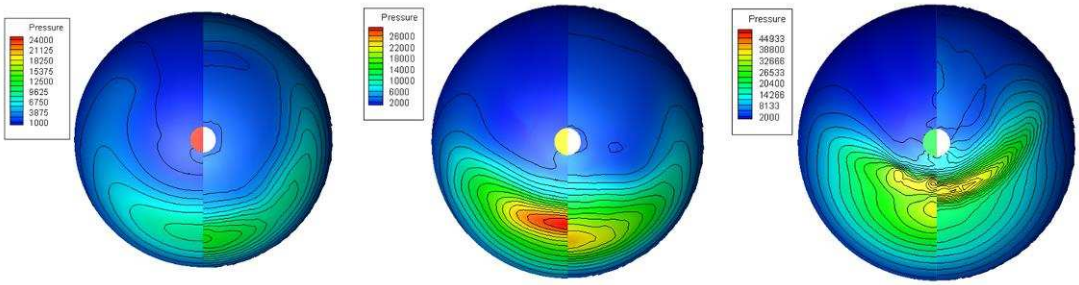

（a）α=4º　　（b）α=8º　　（c）α=12º

Fig. 9 Pressure distribution on the surface varied with angle of attack(left: with aerospike; right: with counterflowing jet).

Fig. 10 shows the comparison of density distributions of noses with aerospike and counterflowing jet with variable angle of attack in symmetrical plane. The recirculation region beside the windward generatrix is pushed upward by the incoming flow with the increasing angle of attack, and the recirculation region beside the leeward generatrix is dragged to the backside for both models.

For the nose with aerospike, it is easy to distinguish three shock waves formed by the presence of the aerospike, the bow shock, separation shock and the reattachment shock, on the windward generatrix, the recompression shock wave becomes stronger with the increasing angle of attack, an extra high pressure region is formed behind it. For the nose with counterflowing jet, the jet forms a series of Mach diamonds, penetrates the bow shock, and modifies it significantly to an expansion shock, which is the typical characteristics of LPM, as shown in Fig. 10(a).

It is interesting to find that the flow structure of the LPM jet is sustained in terms of jet penetration and shock dispersion even at angle of attack of 8 degree, while flow asymmetry persisted and became stronger with the increasing angle of attack, the distance between the bow shock and the central point

of the nose surface significantly shorten at angle of attack of 12 degree. The position of reattachment point moves towards to the vertex of the nose.

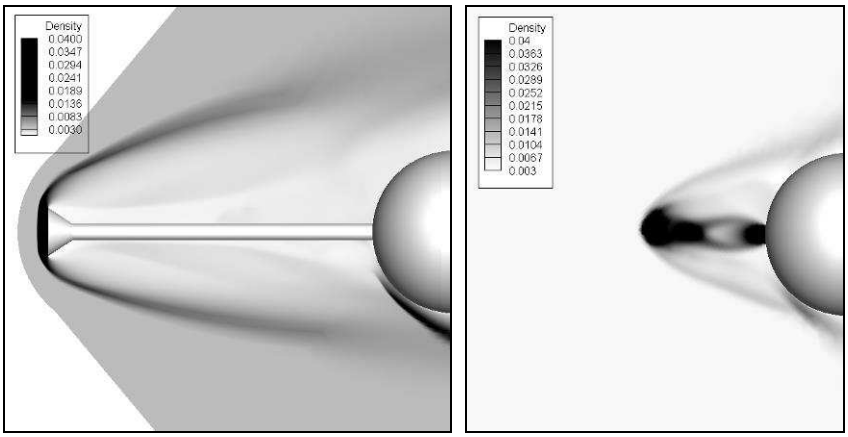

(a) α=4°

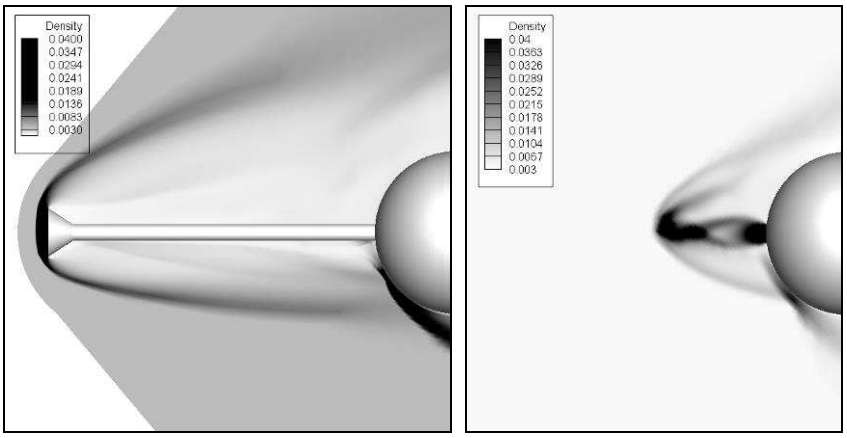

(b) α=8°

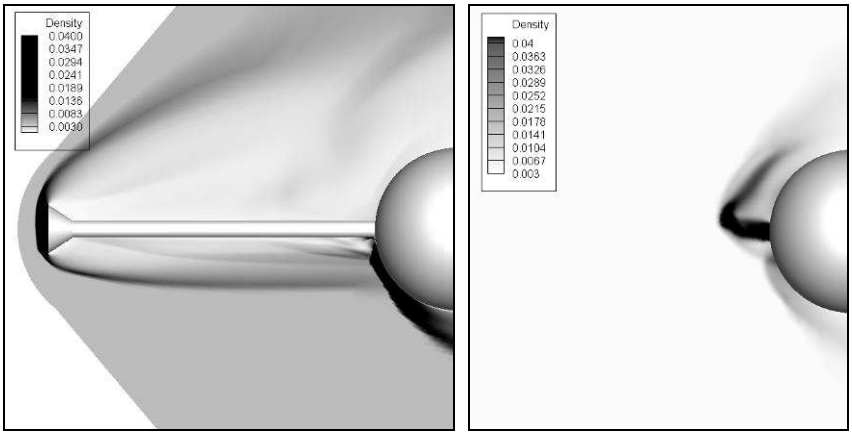

(c) α=12°

Fig. 10 Comparison of density distributions of noses with aerospike and counterflowing jet with variable angle of attack in symmetrical plane.

3.2 Drag reduction effect

Similar to the drag reduction principle of aerospike, the most effective way to reduce drag using a

LPM counterflowing jet is to achieve the maximum jet penetration and to create both a slender displacement shape and multiple enveloping shock waves in the hypersonic oncoming stream.

For model with aerospike, it is necessary to consider the drag of aerospike when evaluating its drag characteristics. As Table 2 shows, at angle of attack of zero degree, the drag forces of nose D_0 and aerospike D_s are 11.65 N and 15.91 N, respectively. This calculation is more complex for counterflowing jet because of the existence of jet thrust T_j. When calculating the modified drag on the nose, the jet thrust is added to the axial component of the pressure integrated over the nose surface. D_T is the total drag force with jet including the drag penalty of the counterflowing jet, D_0 is the drag force of the nose and $\bar{D}$ is the non-dimensional drag force that divided by the drag of nose without jet. The jet thrust for producing of counterflowing jet :

$$T_j = \dot{m}V_j + A_j(P_j - P)$$

is calculated, where $\dot{m}$ is mass flow rate of the jet, V_j is the velocity at the jet exit, A_j is the area of jet exit. The jet thrust is T_j = 5.21 N, and it is about 16.50% of the total drag of the nose, while the drag of aerospike accounts for 57.73% of the total drag of the nose. The results shows that the two methods can effectively reduce drag force compare to the drag of baseline model's nose, and the non-dimensional drag of nose with aerospike is slightly less than that of the counterflowing jet at angle of attack of zero degree.

Table 2 Comparison of drag force of different models' noses (α=0°)

	D_0/(N)	$\dot{m}$/(kg/s)	T_j/(N)	D_s/(N)	D_T/(N)	$\bar{D}$
Baseline model	92.71	-	-	-	92.71	1
Model with aerospike	11.65	-	-	15.91	27.56	0.30
Model with counterflowing jet	26.37	0.0068	5.21	-	31.58	0.34

The variations of the drag of the nose and the whole model with angle of attack are shown in Fig.11. Taking the baseline model as a reference, the maximum drag reduction effect is obtained for the two models' noses at angle of attack of zero degree, drag reduction for nose with aerospike is about 70% and for nose with counterflowing jet is about 66%.

The drag of the baseline model's nose remain almost the same with the increasing of angle of attack, and the drag of nose with aerospike and counterflowing jet rapidly increases with angle of attack, but there are some differences between the two trends, the drag of nose with aerospike linearly growth with the increase of angle of attack while the drag of nose with counterflowing jet increases slowly within

angle of attack of 8 degree, then the drag increases quickly when angle of attack is greater than 8 degree. This feature can also be found in Fig. 11(b), and the drag of model with counterflowing jet is less than that of model with aerospike between 6 degree and 8 degree. This is visible from local enlarged curves, and an obvious drag reduction effect in the range of small angle of attack is observed. The value is 7.25% for model with aerospike and 8.80% for model with counterflowing jet at angle of attack of 6 degree.

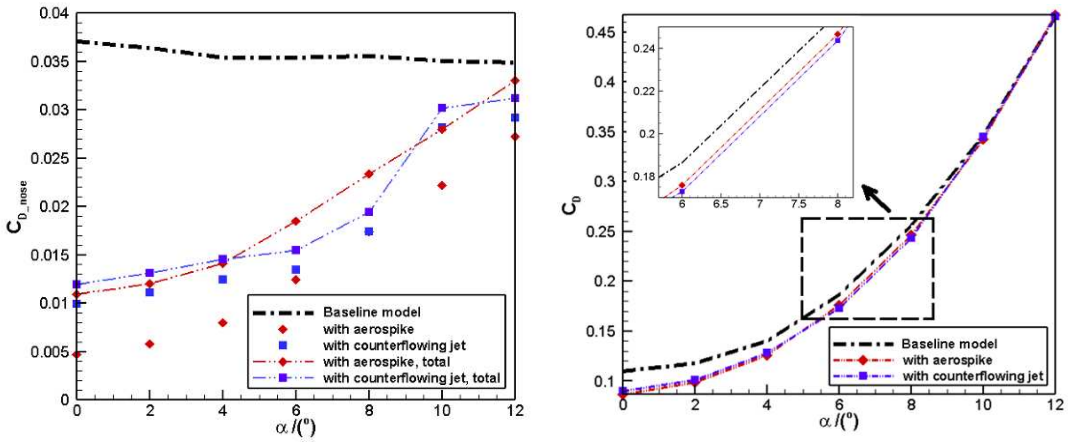

(a) The nose (b) The whole model

Fig. 11 Drag coefficient varies with angle of attack.

Also from previous research [44], it was observed that even with smaller angles of attack (< 5°), the long penetration mode vanishes rapidly. Jiang et al. [45] argued that even a 2° attack angle will cause large reduction of its performance. However, Daso et al. [43] observed that the LPM jet can be present even for angles of attack up to 10°. In this paper, we prove that by suitably designing the geometric shape of nozzle exit and PR, the effective application range of counterflowing jet technology could cover the flying angle of attack of hypersonic lifting-body vehicles.

The aerodynamic characteristics of three models are compared in Fig. 12. The maximum lift-to-drag ratio is obtained at 6 degree for all models, and this values of models with aerospike and counterflowing jet are almost the same as that obtained by the baseline model when α>10º, which means that the two methods have no drag reduction effect when angle of attack is larger than 10 degree. When angle of attack is α=6º, The lift-to-drag ratio increase of model with aerospike and model with counterflowing jet is 5.53% and 6.96%, respectively. The lift-to-drag ratio of model with counterflowing jet is 3.58, compared to 3.34 of the baseline model.

As shown in Table 2, mass flow rate of the counterflowing jet is 0.0068 kg/s, supposing a gliding vehicle with Ma 8 cruising at a height of 40 km, it takes about 13 minutes to complete a range of 2000

kilometers, by using counterflowing jet as a drag reduction concept, the range could be increased about 7%, costing an extra weight about 5.3 kilograms of jet gas, which is almost negligible compared with the weight of a whole vehicle.

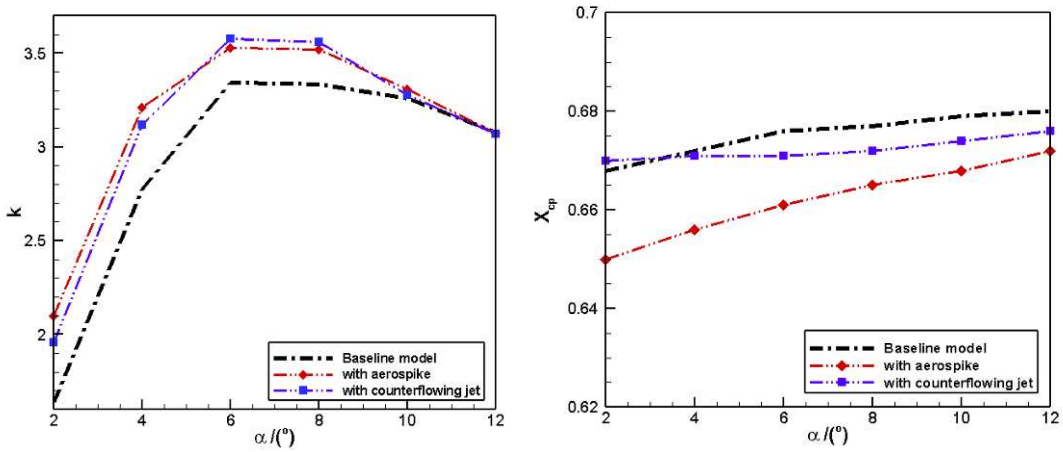

(a) Lift-to-drag ratio (b) Center of pressure coefficient

Fig. 12 Aerodynamic characteristics vary with angle of attack.

As shown in Fig. 12(b), it's interesting to note that, compared with the baseline model, the displacement of the center of pressure decreases from 1.2% to 0.6% when counterflowing jet is used, while this value of model with aerospike increases to 2.2% in the range of angle of attack, and what's more, the position of center of pressure shifts towards to the head of the vehicle, reducing the longitudinal stability of the vehicle. Based on the comparison mentioned above, it can be concluded that the performance of counterflowing jet is better than aerospike considering of lift-to-drag ratio and center of pressure shifting for hypersonic vehicle at the cruising angle of attack.

3.3 Periodic oscillation of LPM

As discussed in Section 3.1, Fig. 7 shows that a new displaced shape created by counterflowing jet is more efficient in reducing the wave drag than the blunt nose. As a side effect, the flow field is unsteady with a certain degree of magnitude aerodynamic fluctuation. The LPM is an unstable flowfield characterized by the familiar diamond-pattern jet plume that penetrates into the bow-shock. However, LPM jets only exist for a narrow range of conditions beyond which the jet switches into SPM. Based on previous study, the source of instability of the counterflowing jet interaction was found to be closely related to the behavior of slightly under-expanded free jets. The diamond-shape shock cells from the under-expanded jets cause strong flow instability as the jet plume interacts with opposing freestream.

From the view of Venkatachari et al. [46], the source of instability of the counterflowing jet

interaction was found to be closely related to the behavior of slightly under-expanded free jets. The diamond-shape shock cells from the under-expanded jets cause strong flow instability as the jet plume interacts with opposing freestream. Bilal and Lu [47] carried out a computational study of the counterflowing jet by a cold supersonic jet from a hemispherical cylinder at four different hypersonic freestream flows, and they investigated the oscillatory LPM flow regime for drag reduction. Chang et al. [48] focused on time-accurate numerical computations of hypersonic flows over a set of capsule configurations, which employ a counterflowing jet to offset the detached bow shock, by adding different counterflowing jet exit Mach number, unsteady oscillations in the drag is studied. Rockwell and Naudascher [49] studied the mechanism and pointed out, when the injecting pressure or more appropriately the injecting mass flow rate is less than a critical value, the jet-shock interaction will initiate an oscillatory flow motion through the feedback loop of the free shear layer instability. A general explanation for this self-sustaining unsteadiness and oscillation is that it may be resulted from the pressure perturbation in the free shear layer which will propagate upstream to the Mach disk though the subsonic recirculation zone due to adverse pressure gradient.

On the basis of previous researches, the detailed drag result and flow structure of LPM are obtained by solving the time-dependent Navier-Stokes equations. In order to explore the oscillating characteristic of the counterflowing jet with the maximum lift-to-drag ratio of the model, 6 degree is chosen as the employed angle of attack. The simulation results of the nose with counterflowing jet are analyzed in terms of drag coefficient and are presented in Fig. 13. The figures reveal a typical feature, namely periodic oscillation of a flow around the nose. The data evaluating the aerodynamic characteristics of the model is derived from the instantaneous drag coefficient, and the fixed value is obtained by averaging the instantaneous drag by time.

The time history of the drag coefficient clearly exhibits a low frequency, large-amplitude oscillation. It can be calculated from Fig.13 that the oscillation frequency is 444Hz. Shang [35][50] studied experimentally supersonic injection from a hypersonic blunt body for drag reduction, and spectral data of drag measurements showed that two dominant discrete frequencies of 100 and 440 Hz are clearly revealed. This frequency is similar to that obtained in this paper. According to the variable trend of drag coefficient of the nose, a period can be divided into six typical stages, which can be seen judged from the local enlarged image.

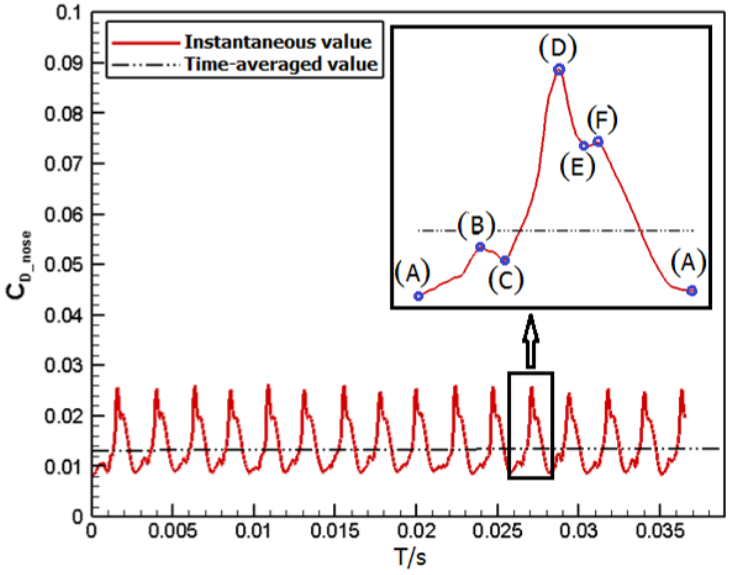

Fig. 13 Time history of the drag coefficient on the nose of the model.

Fig. 14 shows the centerline Mach number distributions ahead of the nose during the whole cycle of bow shock oscillation. The X= 0 location is the center point on the nozzle exit. It is evident that the jet structure for LPM has multibarrel shock structure with two expansion zones. The shock stand-off distance reaches a peak value at stage A, and the bow shock is at maximum position, which is 72.8mm, as Table 3 shown, and then begins to drop drastically due to unsteady nature of the flow mode, until it reaches the minimum value at stage D, the shock stand-off distance is 30.3mm. Beyond this stage, the bow shock reverses its direction to move in the direction of the counterflowing jet, indicating a tendency for the jet to expand, and it increases slowly to complete an oscillation cycle.

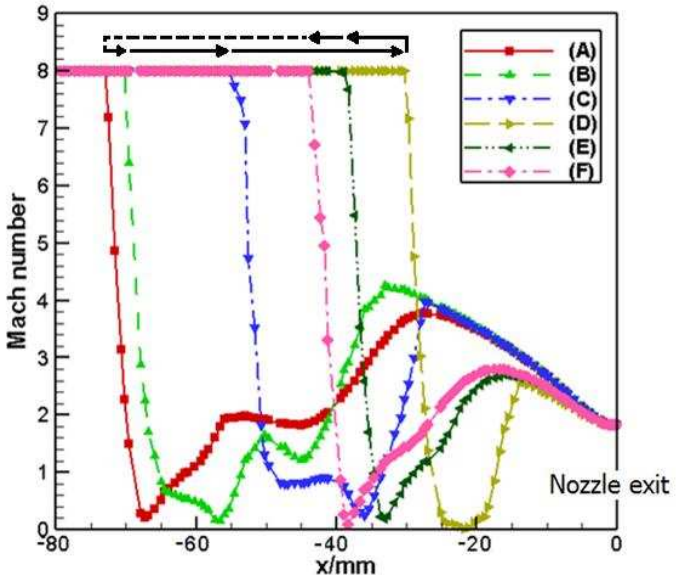

Fig. 14 Shock stand-off distance across the jet centerline/axis for one cycle.

Table 3 Shock stand-off distance for different stages of one cycle

stages	A	B	C	D	E	F
Shock stand-off distance/mm	72.8	70.2	55.3	30.3	38.9	43.9

An illustration of instantaneous density distributions showing many more complex details about the flow structure is illustrated below in Fig. 15. For ease of comparison and to maintain consistency, the same color range is used in the presentation for the density parameter. From stage A to stage F, the evolving flow field due to counterflowing jet ejection field over a 0.00157 second can be observed. The shock shape is asymmetric due to the pronounced characteristic unsteadiness and oscillations in the longitudinal plane. The jet is almost fully expanded, creating a multi-shock wave structure, as shown at stage A. As the time increased, instability of flow field causes the deflection of the top of shock structure. At the same time, the shock-off distance decreases, the structure of the flow field changed to SPM jet, as shown at stage D. The shock structure maintains almost steady after that stage, finishing the oscillation through a feedback mechanism.

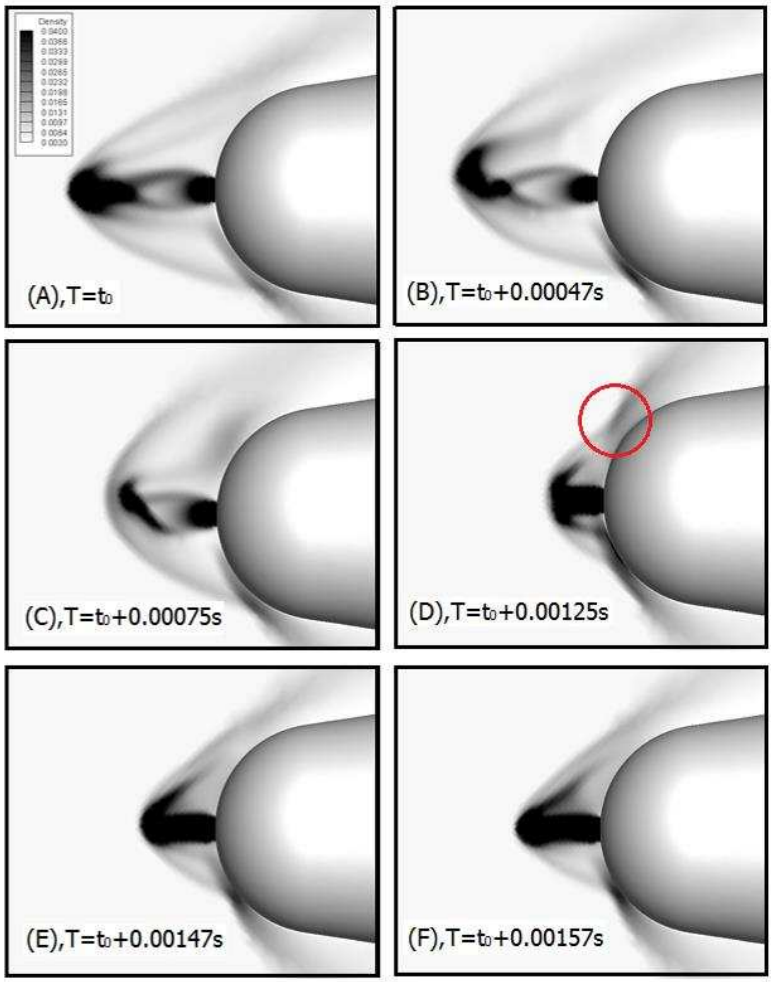

Fig. 15 Instantaneous density distributions of a typical cycle of LPM oscillations.

Non-dimensional pressure distributions on the nose of a cycle are shown in Fig. 16, and the values come from the symmetry plane of the nose. Although the maximum drag of the nose is obtained at stage D, the peak of pressure on the windward side of the nose at this stage is not the largest. This interesting phenomenon could be explained by Fig. 16(b). As the figure shown, there is a dramatic increase of the pressure on the leeward side of the nose at stage D, and almost 2 to 3 times larger than that of other stages. However, these results originate from pressure distributions of the symmetry plane. In order to conduct a comprehensive analysis, pressure distributions on the nose surface of a cycle are required.

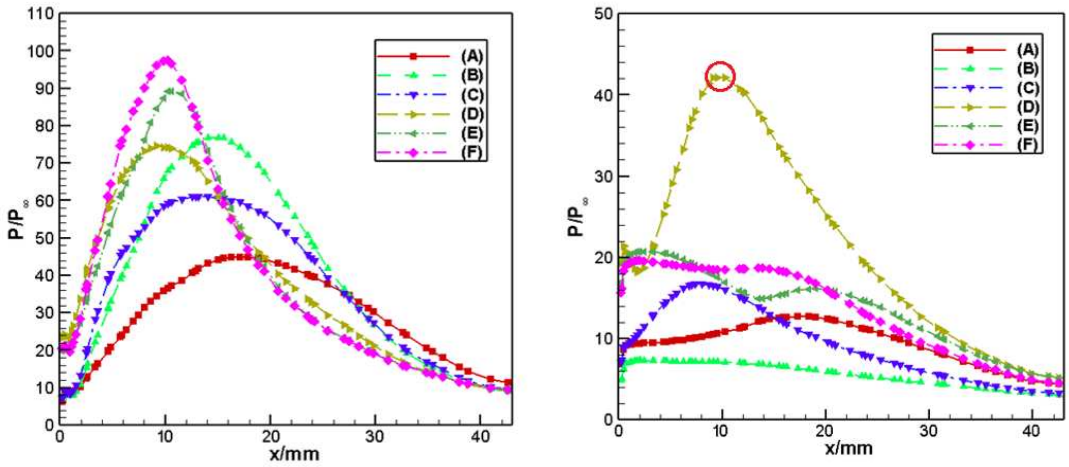

(a) windward side (b) leeward side

Fig. 16 Non-dimensional pressure distributions on the nose for one cycle.

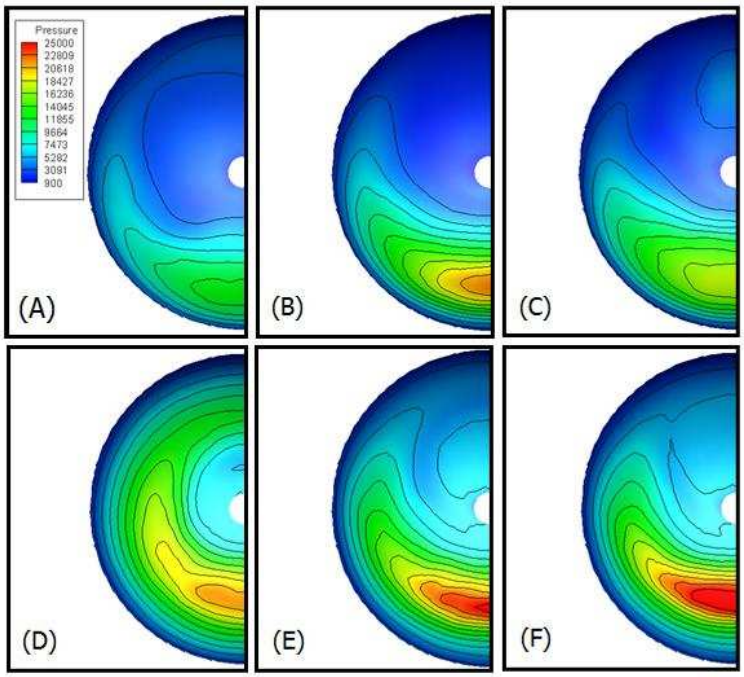

Fig. 17 Instantaneous pressure contours on the nose for one cycle.

Fig. 17 shows instantaneous pressure contours on the nose for a complete cycle of bow shock oscillation. The same color range is used in the presentation for the pressure contours. At stage D, the bow shock is at minimum stand-off distance resulting in increase in the pressure distribution on both sides of the nose in the longitudinal plane, not only the low pressure recirculation zone of windward becomes smaller, but also a high pressure area appears on the leeward of the nose, resulting the maximum value of pressure, which could finally explain the cause of the maximum drag of the nose.

4. Conclusions

Computational analyses have been performed to investigate the potential benefits of both passive and active flow control concept using aerospike and counterflowing jet to modify the external flowfields of the nose and strongly weaken or disperse the shock waves to significantly reduce drag and improve aerodynamic performance of the whole vehicle. Special attention was also given to understanding the unstable oscillation phenomenon of counterflowing jet known as LPM and the oscillation characteristics of a complete period are obtained. The following conclusions are made from the results.

(1) The flow structure and pressure distribution results showed an obvious decrease in shock-wave amplitude and pressure values of the nose for both models with aerospike and counterflowing jet, and the counterflowing jet shows better effects than the aerospike in reducing the peak values of pressure and reducing the area of high pressure at angle of attack.

(2) Drag reduction for nose with aerospike is about 70% and for nose with counterflowing jet is about 66% at angle of attack of 0 degree, and the drag of model with counterflowing jet is less than that of model with aerospike at angle of attack representing cruising conditions of the vehicle. The value of drag reduction is 7.25% for model with aerospike and 8.80% for model with counterflowing jet at angle of attack of 6 degree.

(3) Flow structure of the counterflowing jet is sustained in terms of jet penetration and shock dispersion even at angle of attack of 8 degree, which means that, by suitably designing the geometric shape of nozzle exit and PR, the effective application range of counterflowing jet as an active flow control technology could cover the flying angle of attack of hypersonic gliding vehicle.

(4) The LPM counterflowing jet results in a significant increase of the bow shock stand-off distance,

accompanied by strong flow unsteadiness. The oscillation frequency of LPM jet is 444Hz at angle of attack of 6 degree. Due to the instability of the flow field, the multibarrel shock structure collapses into a Mach disk at stage D, showing a typical SPM features.

Although the aerospike as a passive flow control concept has almost the same drag reduction effect as counterflowing jet, the spike tip would be damaged due to high temperature behind the shock during a long-range flight. Thus, it would not have high reusability. In contrast, the jet flow of the counterflowing jet protects the nozzle exit from the high temperature region, only less energy and small installation space in the nose of the vehicle are required. Therefore, the counterflowing jet has more advantages than the aerospike for a long-range gliding hypersonic vehicle. In the following study, the emphasis is the feasibility of adjusting jet direction, which can further broaden the scope of the use of counterflowing jet as an innovative drag reduction technique.

Acknowledgments

The authors would like to thank the Aerospace International Innovation Talent Cultivation Project (AIITCP) of Program China Scholarship Council (CSC) and the National Natural Science Foundation of China (No. 11502291) for their support.

References

[1]. Crawford D H. Investigation of the flow over spiked-nose hemisphere-cylinder at Mach Number of 6.8. NACA,1959,6(1):112-118.

[2]. Gauer M, Paull A. Numerical Investigation of a Spiked Blunt nose cone at Hypersonic speeds. Journal of Spacecraft and Rockets,2008, 45(3):459-471.

[3]. Guy Y, McLaughlin T E, Morrow J A. Blunt body wave drag reduction by means of a standoff spike. AIAA Journal,2001,32(7):588-599.

[4]. Farr R A, Chang C L, Jones J H, et al. On the Comparison of the Long Penetration Mode (LPM) Supersonic Counterflowing Jet to the Supersonic Screech Jet//21st AIAA/CEAS Aeroacoustics Conference. 2015-3126.

[5]. Daso E O, Beaulieu W, Hager J O, et al. Prediction of drag reduction in supersonic and hypersonic flows with counterflow jets. AIAA 2002-5115, 2002.

[6]. Li S B, Wang Z G, Barakos G N, Huang W, Steijl R. Research on the drag reduction performance induced by the counterflowing jet for waverider with variable blunt radii. Acta Astronautica, 2016, 127: 120-130

[7]. Markhotok A. A mechanism of wave drag reduction in the thermal energy deposition experiments. Physics of Plasmas (1994-present), 2015, 22(6): 063512.

[8]. Jiang Z, Liu Y, Han G. Conceptual study on non-ablative TPS for hypersonic vehicles//17th AIAA International Space Planes and Hypersonic Systems and Technologies Conference. 2011: 2372.

[9]. Huang W, A survey of drag and heat reduction in supersonic flows by a counterflowing jet and its combinations. J. Zhejiang Univ.-Sci. A (Appl. Phys. Eng.) 16(2015) 551–561.

[10]. Wang Z G, Sun X W, Huang W, Li S B, Yan L. Experimental investigation on drag and heat flux reduction in supersonic/hypersonic flows: A survey. Acta Astronautica, 2016, 129: 95-110

[11]. Huang W, Ma L, Wang Z G, Pourkashanian M, Ingham D B, Luo S B, Lei J. A parametric study on the aerodynamic characteristics of a hypersonic waverider vehicle. Acta Astronautica, 2011, 69: 135-140

[12]. Mair W A. Experiments on separation of boundary layers on probes in front of blunt-nosed bodies in a supersonic air stream. The London, Edinburgh, and Dublin Philosophical Magazine and Journal of Science, 1952, 43(342): 695-716.

[13]. Maull D J. Hypersonic flow over axially symmetric spiked bodies. Journal of Fluid Mechanics, 1960, 8(04): 584-592.

[14]. Wood C J. Hypersonic flow over spiked cones. Journal of Fluid Mechanics, 1962, 12(04): 614-624.

[15]. Chapman D R, Kuehn D M, Larson H K. Investigation of separated flows in supersonic and subsonic streams with emphasis on the effect of transition. 1958. NACA TR 1356; 1957.

[16]. Ahmed M, Qin N. Drag reduction using aerodisks for hypersonic hemispherical bodies. Journal of Spacecraft and Rockets, 2010, 47(1): 62-80.

[17]. Ahmed M Y M, Qin N. Recent advances in the aerothermodynamics of spiked hypersonic vehicles. Progress in Aerospace Sciences, 2011, 47(6): 425-449.

[18]. M. Ahmed M Y, Qin N. Surrogate-based multi-objective aerothermodynamic design optimization of hypersonic spiked bodies. AIAA Journal, 2012, 50(4): 797-810.

[19]. Asif M, Zahir S, Kamran N,et al. Computational Investigations aerodynamic force at

supersonic/hypersonic flow past a blunt body with various forward facing spikes. AIAA Journal, 2004, 6(1):5189-5194.

[20]. Srulijes J, Gnemmi P, Runne K,et al. High-pressure shock tunnel experiments and CFD calculations on spike-tipped blunt bodies. AIAA Journal,2002,5(1):2918-2926.

[21]. Huang W, Liu J, Xia Z X. Drag reduction mechanism induced by a combinational opposing jet and spike concept in supersonic flows. Acta Astronautica, 2015, 115: 24-31

[22]. Motoyama N, Mihara K, Miyajima R, et al. Thermal protection and drag reduction with use of spike in hypersonic flow. AIAA paper, 2001, 1828: 2001.

[23]. Mehta R C. Flow field computations over conical, disc and flat spiked body at Mach 6. AIAA paper, 2009, 325: 2009.

[24]. Tahani M, Karimi M S, Motlagh A M, et al. Numerical investigation of drag and heat reduction in hypersonic spiked blunt bodies. Heat and Mass Transfer, 2013, 49(10): 1369-1384.

[25]. Kalimuthu R, Mehta R C, Rathakrishnan E. Experimental investigation on spiked body in hypersonic flow. Aeronautical Journal, 2008, 112(1136): 593-598.

[26]. Yadav R, Guven U. Aerothermodynamics of a hypersonic projectile with a double-disk aerospike. Aeronautical Journal, 2013, 117(1195): 913-928.

[27]. Schülein E. Wave drag reduction concept for blunt bodies at high angles of attack//Shock waves. Springer Berlin Heidelberg, 2009: 1315-1320.

[28]. Huang W, Yan L, Liu J, Jin L, Tan J G. Drag and heat reduction mechanism in the combinational opposing jet and acoustic cavity concept for hypersonic vehicles. Aerospace Science and Technology, 2015, 42: 407-414

[29]. Li S B, Wang Z G, Huang W, Liu J. Drag and heat reduction performance for an equal polygon opposing jet. Journal of Aerospace Engineering, 2017, 30(1): 04016065

[30]. Finley P J. The flow of a jet from a body opposing a supersonic free stream. Journal of Fluid Mechanics, 1966, 26(02): 337-368.

[31]. Romeo D J, Sterrett J R. Exploratory investigation of the effect of a forward-facing jet on the bow shock of a blunt body in a Mach number 6 free stream. National Aeronautics and Space Administration, NASA TN D-1605, 1963.

[32]. Josyula E, Pinney M, Blake W B. Applications of a counterflow drag reduction technique in high-speed systems. Journal of Spacecraft and Rockets, 2002, 39(4): 605-614.

[33]. Li S B, Wang Z G, Huang W, et al. Effect of the injector configuration for opposing jet on the drag and heat reduction. Aerospace Science and Technology, 2016, 51: 78-86.

[34]. Bushnell D M, Huffman J K. Forward Penetration of Liquid Water and Liquid Nitrogen from the Orifice at the Stagnation Point of a Hemispherically Blunted Body in Hypersonic Flow. NASA TM X-1493, 1968.

[35]. Shang J S, Hayes J, Wurtzler K, et al. Jet-spike bifurcation in high-speed flows. AIAA Journal, 2001, 39(6): 1159-1165.

[36]. Shang J S, Hayes J, Menart J. Hypersonic flow over a blunt body with plasma injection. Journal of Spacecraft and Rockets, 2002, 39(3): 367-375.

[37]. Fomichev V P, Fomin V M, Korotaeva T A, et al. Hypersonic Flow Around a Blunted Body with Counterflow Plasma Jet. Institute of Theoretical and Applied Mechanics, Novosibirsk, Russia, 2002:51-55.

[38]. Kulkarni V, Hegde G M, Jagadeesh G, et al. Aerodynamic drag reduction by heat addition into the shock layer for a large angle blunt cone in hypersonic flow. Physics of Fluids (1994-present), 2008, 20(8): 081703.

[39]. Aruna S, Anjalidevi S P. Computational study on the influence of jet on reduction of drag over cone flare bodies in hypersonic turbulent flow. Procedia Engineering, 2012, 38: 3635-3648.

[40]. Huang W, Liu W D, Li S B, Xia Z X, Liu J, Wang Z G. Influences of the turbulence model and the slot width on the transverse slot injection flow field in supersonic flows. Acta Astronautica, 2012, 73: 1-9

[41]. Huang W, Li S B, Yan L, Wang Z G. Performance evaluation and parametric analysis on cantilevered ramp injector in supersonic flows. Acta Astronautica, 2013, 84: 141-152

[42]. Kalimuthu R, Mehta R C, Rathakrishnan E. Experimental Investigation on Spiked Body in Hypersonic Flow. Aeronautical Journal, 2008, 112(1136): 593-598.

[43]. Daso E O, Pritchett V E, Wang T S, et al. The dynamics of shock dispersion and interactions in supersonic freestreams with counterflowing jets. AIAA Journal, 2009, 47(6): 1313-1326.

[44]. Romeo, D. and Sterrett, J., Exploratory Investigation of the Effect of a Forward-Facing Jet on the Bow Shock of a Blunt Body in a Mach Number 6 Free Stream. NASA TN D-1605, February 1963.

[45]. Jiang Z L, Liu Y, Han G. Conceptual Study on Non-ablative TPS for Hypersonic Vehicles, AIAA

2011-2372,2011.

[46]. Venkatachari B S, Ito Y, Cheng G, et al. Numerical investigation of the interaction of counterflowing jets and supersonic capsule flows. AIAA Paper, 2011-4030，2011.

[47]. Bilal Hussain Shah S, Lu X Y. Computational study of drag reduction at various freestream flows using a counterflow jet from a hemispherical cylinder. Engineering Applications of Computational Fluid Mechanics, 2010, 4(1): 150-163.

[48]. Chang C L, Venkatachari B S, Cheng G. Effect of Counterflow Jet on a Supersonic Reentry Capsule. AIAA, 2006-4776, 2006.

[49]. Rockwell D, Naudascher E. Self-sustained oscillations of impinging free shear layers. Annual Review of Fluid Mechanics, 1979, 11(1): 67-94.

[50]. Shang J S. Plasma injection for hypersonic blunt-body drag reduction. AIAA Journal, 2002, 40(6): 1178-1186.